Source-Scaling Relationship for M 4.6–8.9 Earthquakes, Specifically for Earthquakes in the Collision Zone of Taiwan

by Yin-Tung Yen and Kuo-Fong Ma

Abstract   We investigated the source scaling of earthquakes (M_w 4.6–8.9), mostly from the Taiwan orogenic belt, and made a global compilation of source parameters to examine the scaling self-similarity. Finite-fault slip models (12 dip-slip and 7 strike-slip) using mainly dense strong-motion data and teleseismic data from Taiwan were utilized. Seven additional earthquakes ($M > 7$) were included for further examination of scaling of large events. We determined the effective length and width for the scaling study was $M_0 \sim L^2$ and $M_0 \sim L^3$ for the events less than and larger than the seismic moment of 10^{20} N m, respectively, regardless of the fault types, suggesting a nonself-similar scaling for small to moderate events and a self-similar scaling for large events. Although the events showed variation in stress drops, with the exception of three events with high stress drops, most of the events had stress drops of 10–100 bars. The observed bilinear relation is well explained by the derived magnitude–area equation of Shaw (2009) when we considered only events with stress drops of 10–100 bars and a seismogenic thickness of 35 km. The bilinear feature of the regressed magnitude–area scaling holds for ruptured areas up to about 1000 km² for our seismogenic thickness of 35 km. For the events having rupture areas larger than that, the average slip becomes proportional to the rupture length. The distinct high stress drop events from blind faults in the western foothill of Taiwan yield local high peak ground accelerations (PGAs) when compared to the Next Generation Attenuation model. Regardless of the relative small magnitudes of these events, the high PGAs give the region higher seismic hazard potential and thus require special attention for seismic hazard mitigation.

Introduction

In the past several decades, several studies have been carried out to investigate the source scaling of earthquakes for understanding the macroscopic self-similarity of earthquakes. Source-scaling relationships not only provide an insight into the underlying mechanics of the rupture process but also give deterministic parameters for ground-motion prediction for earthquake hazard mitigation. In general, the earthquake source dimensions can be inferred from field surveys for large earthquakes and aftershock patterns for large and small earthquakes. Numerous relationships among fault length (L), fault width (W), fault area (A), and mean displacement (D) corresponding to seismic moment (M_0) were established by Wells and Coppersmith (1994); they provided the empirical relationships for predetermining source parameters for various earthquake sizes. The scaling relationships suggest that the seismic moment is approximately proportional to the square of fault length and that rupture width is independent of rupture length for large earthquakes, which support the L model proposed by Scholz (1982), in which stress drop and mean slip are predominated by fault length (Wang and Ou, 1998). The study by Pegler and Das (1996) defining fault length from aftershock pattern suggests a similar scaling relationship for strike-slip crustal earthquakes. However, Romanowicz (1992) provided a relationship of $M_0 \sim L$ for very large earthquakes, suggesting that mean slip is related to fault width, not fault length. The idea of whether mean slip scales to width or length is still controversial (Romanowicz, 1992; Scholz, 1994). Distinct scaling of M_0 to L, $M_0 \sim L^3$ for small earthquakes, and $M_0 \sim L^2$ for larger earthquakes were found by Shimazaki (1986), but scaling for the whole data set still maintains a relationship of $M_0 \sim L^3$. Insufficient coverage of comprehensive seismic moment may lead to to better determine scaling over a range of sizes. Regardless of the type of focal mechanisms and the size of earthquakes, there is a relationship of $M_0 \sim L^3$, but, when only considering the large strike-slip earthquakes, the relationship is $M_0 \sim L^2$, assuming a constant stress drop. However, the thickness of the seismogenic zone seems to play a significant role for the difference of scaling between small and large earthquakes (Pacheco *et al.*,

1992). For very large, large, and small earthquakes, M_0 is proportional to L, L^2, and L^3 because fault width is dependent on the thickness of the seismogenic zone, and there is an aspect ratio of the fault length to the fault width (Yin and Rogers, 1996). In the case of small earthquakes, the source dimension might tend to be overestimated because of the uncertainty in the aftershocks' location and the temporal extension of the aftershock region. The different scaling relationships shown thus far in this paper might also come from different tectonic settings, which influence the source rupture process.

The source parameters, including rupture length, rupture width, and mean slip, have now been validly resolved by finite-fault slip models from the earthquake source inver-

sions. Through the definition on effective fault dimensions from the autocorrelation of the slip function from the slip models, Mai and Beroza (2000) suggested that the self-similar scaling is broken for large strike-slip events, which might be related to the strong influence of the finite seismogenic width of the fault zone.

The dense strong-motion stations in Taiwan (Fig. 1), a region with high seismicity, allow us to carry out finite-fault slip modeling for a wide range of earthquakes with magnitudes down to M_w 4.6. In view of the debate on the source scaling of small to large earthquakes and the association to the fault types, we collected the well-resolved slip models from the finite-fault inversion in the Taiwan region and deployed the same definition of effective fault dimension
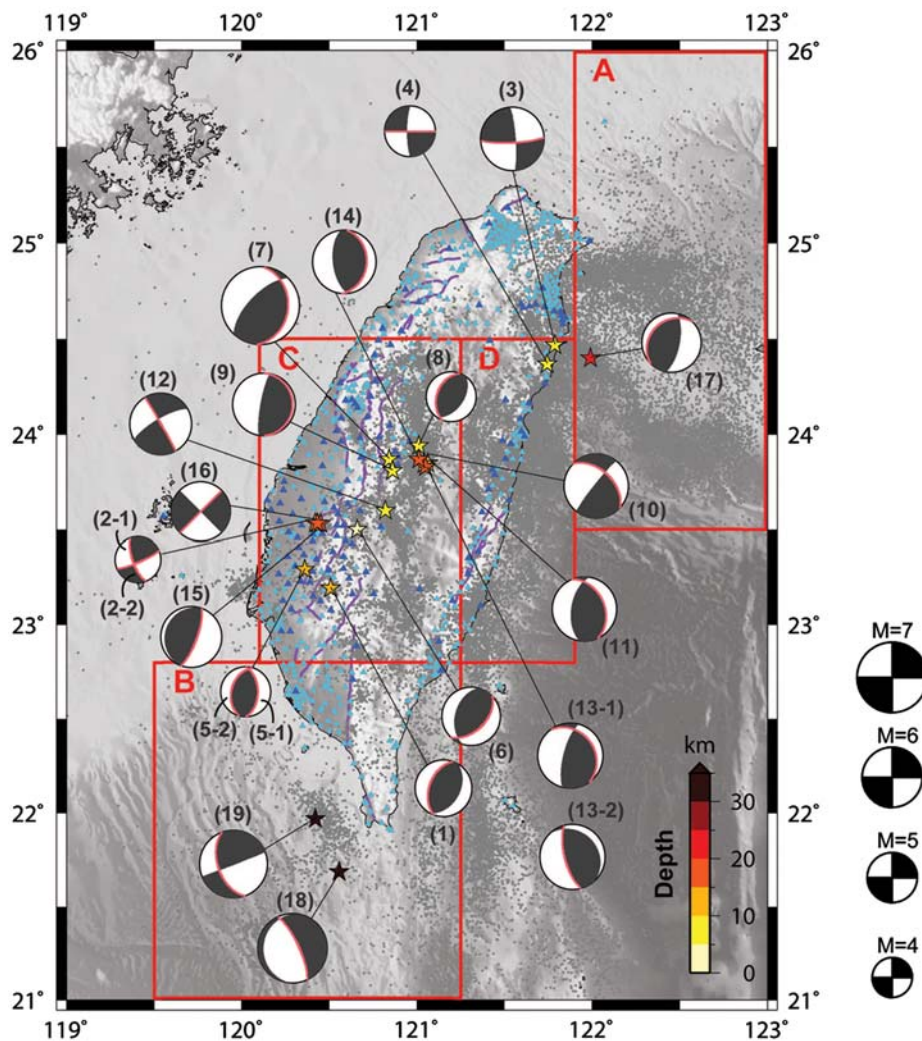

Figure 1. The distribution of earthquakes and their corresponding focal mechanisms used in this study. The thick line marked on the focal mechanism indicates the rupture plane from the references as indicated by the number in the parentheses listed in Table 1. The shading scale on the stars represents the hypocentral depth, as shown in the legend. The study area was divided into four regions (A, B, C, and D) for examining the distribution of the seismicity in the individual regions in Figure 6. The background seismicity is shown by dots for the time period from January 1990 to December 2007 for $M_L > 3$. The active faults (lines), identified by Central Geological Survey (CGS) of Taiwan, are also shown. The open and solid triangles show the distribution of the Taiwan Strong Motion network, and the solid triangles are the stations used in the finite-fault model inversions. The color version of this figure is available only in the electronic edition.

as Mai and Beroza (2000) to investigate the source scaling between source parameters (fault length, fault width, and mean slip) with seismic moment to verify the scaling invariance. Our results show the scaling of $M_0 \sim L^2$ and $M_0 \sim L^3$ for the small–moderate and large events, respectively, and the seismogenic thickness controls the evolution of slip.

Characterizing Slip Models for Source Parameters

To construct the scaling relationship of the source parameters, we compiled slip models of 19 moderate-to-large earthquakes in the Taiwan region from a finite-fault inverse algorithm mainly using dense strong-motion data and teleseismic data from several investigators (Table 1). The slip models of the 19 events utilized a similar inversion scheme developed by Hartzell and Heaton (1983). In general, the frequency band used in these data sets for the finite-fault inversion algorithm is from 0.01 to 1 Hz. Hartzell and Heaton (1983) showed that the slip models inverted from teleseismic and/or strong-motion data reveal similar slip patterns, with a possible difference in resolution, as also intensively discussed by several other investigators (e.g., Mendoza and Hartzell, 1989; Wald et al., 1991; Wald and Heaton, 1994). In order to give a consistent definition of fault dimension through different finite-fault models for this study, we adopted the spatial autocorrelation scheme of Mai and Beroza (2000) to define the effective fault dimension on length and width to minimize the ambiguity of the determination of fault dimension among different slip models.

Figure 1 shows the distribution of the earthquakes with their focal mechanisms. Detailed information on the locations of events and the mechanism of the identified slip plane, along with the cited references, is listed in Table 1. The slip plane of the earthquake was determined by comparing the waveforms or the aftershock distribution as described in the cited references. If no specific slip plane could be identified, as with events 2 and 5, the slip models from the two fault planes were both analyzed in our studies. For events that have different results in slip plane identification from difference references (e.g., event 13), the proposed slip planes of the different investigators were considered. Though the 1999 Chi-Chi earthquake had been investigated by several different studies (Ma et al., 2001; Wu et al., 2001; Zeng and Chen, 2001), we adopt only the slip model inferred by Ma et al. (2001) because it combined the most complete data set from strong-motion, teleseismic, and Global Positioning System data. The events we studied included 12 dip-slip (reverse, normal, and oblique type events are categorized into the dip-slip category) and 7 strike-slip earthquakes. Their magnitudes ranged from M_w 4.6 to M_w 7.7, which correspond to seismic moments of 7.75×10^{15} to 4.7×10^{20} N m (estimated from referred slip models; Table 1). Fourteen of the events were located in the fold-and-thrust belt of the Taiwan orogenic collision zone.

In general, a rectangular fault dimension was utilized for the finite-fault inversion to accommodate the probable slips over the fault surface. The spatial slip distribution over the fault plane is often heterogeneous. This makes it difficult to determine the fault dimensions (length and width) for the study of scaling relationship among events. Mai and Beroza (2000) defined the effective fault dimension by normalizing the heterogeneity of slip models to reduce the ambiguity on the determination of fault dimensions and average slip. We employ the similar definition of Mai and Beroza (2000) by considering a spatial slip function along the strike direction in which the slips on each subfault along the dip direction were summed. In the same manner, a spatial slip function along the dip was obtained by the summation of slip on each subfault along the strike direction. Furthermore, an autocorrelation method was used to estimate the effective dimension of two spatial functions in the strike and dip directions, respectively. Based on the definition of autocorrelation width (W^{ACF}) by Bracewell (1986), for a given slip function, f, an effective dimension (L_e and W_e) by normalizing the area could be defined under the autocorrelation slip function by the maximum value of autocorrelation function at zero lag (Fig. 2):

$$W^{ACF} = \int_{-\infty}^{\infty} f * f \, dx / f * f|_{x=0} . \qquad (1)$$

Effective mean slip (D_e) was scaled by the formulation from $M_0 = \mu D_e L_e W_e$, where M_0 is the seismic moment derived from the slip model and μ is the rigidity of 3×10^{11} N m^{-2}. Figure 2 shows an example of the estimated effective length and width from the slip model of Ma et al. (2001) of the 1999 Chi-Chi, Taiwan, earthquake. Because there were seven published slip models for the 1999 Chi-Chi earthquake (see Data and Resources section), we examined the difference in the estimated effective fault length and width in different models and determined it to be about 0.2 in the logarithmic scale. The values we adopted in our study are the average values of all the slip models. The derived effective source parameters (L_e, W_e, D_e) for all the events obtained through this analysis are listed in Table 1. As the product of L_e and W_e, A_e is the affected area. The slip distributions of the finite-faults and the corresponding estimation of the L_e and W_e for the events here are shown in Figure A1 of the Appendix.

Source-Scaling Relationships

The scaling relationships of effective fault dimensions (L_e, W_e) and mean slip (D_e) to the seismic moment (M_0) from the referred slip models are shown in Figure 3a–c, respectively. An increasing trend exists when the fault dimensions (Fig. 3a,b) are compared to the seismic moment, but no significant trend was found for mean slip (Fig. 3c). A least-square regression of a linear equation $\log(Y) = a + b \times \log(X)$ shows a slope of $b = 0.47 \pm 0.04$, for the

Table 1
Locations and Corresponding Source Parameters of the Earthquakes Used in This Study

Event No.*	Date (mm/dd/yy in UTC)	Time	Longitude; Latitude (°)	Depth (km)†	M_w	$M_0 \times 10^{18}$ (N m)*	L_e (km)*	W_e (km)*	A_e (km²)*	Av. D_e (cm)*	Stress Drop (bar)	Data*	Strike; Dip; Rake (°)*	Fault Type*	Reference‡
1	12/15/93	09:23	120.507; 23.194	12.50	5.69	0.38	4.88	3.82	18.64	67.95	115.02	SM	200; 48; 84	R	1
2-1	04/06/94	01:12	120.421; 23.533	13.44	4.59	0.0086	0.69	0.97	0.67	42.88	383.21	SM	160; 70; 10	S	1
2-2	04/06/94	01:12	120.421; 23.533	13.44	4.56	0.00775	0.42	0.95	0.40	64.94	752.45	SM	67; 81; 160	S	1
3	06/05/94	01:09	121.787; 24.468	5.30	6.31	3.32	8.85	8.30	73.46	150.66	128.47	SM	87; 81; 8	S	1
4	07/14/95	16:52	121.743; 24.368	8.79	5.11	0.0517	2.43	2.91	7.06	24.41	67.15	SM	270; 90; 10	S	1
5-1	10/31/95	22:27	120.359; 23.291	10.65	4.96	0.0307	1.34	1.40	1.88	54.35	289.46	SM	0; 50; 80	R	1
5-2	10/31/95	22:27	120.359; 23.291	10.65	4.98	0.0332	1.08	1.71	1.84	60.09	323.61	SM	195; 41; 102	R	1
6	07/17/98	04:51	120.660; 23.500	2.80	5.88	0.736	8.13	5.43	44.12	55.61	61.19	SM	45; 50; 110	R	1
7	09/20/99	17:47	120.840; 23.869	8.00	7.75	470	63.02	34.80	2193.35	714.28	111.47	SM + T+G	5; 30; 55	R	2
8	09/20/99	17:57	121.010; 23.940	7.68	5.87	0.715	18.12	17.72	321.10	7.42	3.03	SM	200; 41; 78	R	3
9	09/20/99	18:03	120.860; 23.810	9.75	6.24	2.53	10.89	11.00	119.83	70.38	46.99	SM	0; 10; 80	R	3
10	09/20/99	18:11	121.060; 23.850	12.49	6.47	5.762	20.66	28.18	582.20	32.99	9.99	SM	313; 49; 7	S	4
11	09/20/99	18:16	121.039; 23.844	12.53	6.46	5.445	21.54	20.68	445.45	40.75	14.11	SM	336; 38; 63	R	4
12	09/20/99	21:46	120.820; 23.600	8.57	6.19	2.2	17.39	11.02	191.52	38.29	20.22	SM	330; 89; 15	S	3
13-1	09/22/99	00:14	121.050; 23.830	15.59	6.61	9.096	29.56	28.42	840.10	36.09	9.10	SM	324; 26; 43	R	4
13-2	09/22/99	00:14	121.080; 23.810	12.06	6.23	2.5	17.26	16.31	281.53	29.60	12.89	SM	165; 70; 100	R	3
14	09/25/99	23:52	121.010; 23.870	16.59	6.35	3.7	16.25	15.08	245.08	50.32	23.49	SM	5; 30; 100	R	3
15	10/22/99	02:18	120.450; 23.530	16.59	6.12	1.7	13.87	13.75	190.71	29.71	15.73	SM	20; 75; 90	R	3
16	10/22/99	03:10	120.431; 23.533	16.74	5.90	0.79	3.38	2.86	9.64	273.29	643.44	SM	45; 90; 0	S	1
17	06/09/03	01:52	121.990; 24.40	23.22	5.92	0.865	6.70	7.14	47.84	60.27	63.69	BB	225; 26; 121	R	5
18	12/26/06	12:26	120.555; 21.687	44.11	6.92	27	62.51	70.43	4402.05	20.45	2.25	T	335; 75; −98	N	6
19	12/26/06	12:34	120.420; 21.970	50.22	6.80	18	29.83	24.32	725.45	82.71	22.44	T	160; 52; 2	S	6
1	01/26/01	03:16	70.320; 23.400	20.00	7.38	133	31.63	25.24	798.25	555.38	143.66	T	82; 51; 77	R	7
2	12/26/04	12:58	95.854; 3.316	30.00	8.89	24600	367.17	165.08	60611.82	1352.87	40.16	T	320; 11; 92	R	8
3	05/12/08	06:28	103.364; 30.986	19.00	8.01	1150	243.69	30.62	7460.87	513.79	43.47	T	229; 33; 141	R	9
4	11/14/01	07:28	90.541; 35.946	10.00	7.76	490	318.96	28.46	9078.24	179.92	13.80	T + GS+G	99; 90; −9	S	10
5	01/09/23	02:58	139.200; 35.400	14.60	7.95	933	105.54	60.24	70.00	6357.40	489.19	T + G	290; 25; 138	R	11
6	09/16/78	15:35	57.360; 33.220	5.50	7.09	48.2	74.00	30.10	45.00	2227.03	72.14	T + SM	330; 25; 125	R	11
7	09/19/85	13:17	−102.57; 18.180	17.00	8.01	1150	158.64	115.01	139.00	18245.49	210.10	T + SM	300; 14; 72	R	11

*The events are given by the series of numbers. For events 2 and 5 (for which the ruptured plane is not well identified) or event 13 (which has different preferred fault planes for two slip models), the referred ruptured plane in the individual reference was listed and indicated by number followed by a dashed number. Event numbers shown in bold are for events that occurred outside of Taiwan. M_0, seismic moment from slip models; L_e and W_e, estimated effective fault dimension; A_e, area estimated from effective fault dimension; Av. D_e, mean slip estimated from effective dimension and seismic moment. The data used for the finite-fault inversion of the referred reference: SM, strong-motion data; T, teleseismic data; BB, broadband data; G, geodetic data; GS, geological survey data. The strike, dip, and rake of the identified ruptured plane of the referred reference are also shown. The fault types of the events: R, reverse slip; S, strike slip; N, normal slip.

†Information is from the Central Weather Bureau of Taiwan.

‡1, Ma and Wu (2001); 2, Ma *et al.* (2001); 3, Chi and Dreger (2004); 4, Yen (2002); 5, Lin (2004); 6, Yen *et al.* (2008); 7, Antolik and Dreger (2003); 8, Ammon *et al.* (2005); 9, Ji (2008); 10, Wen *et al.* (2009); 11, Mai and Beroza (2000).
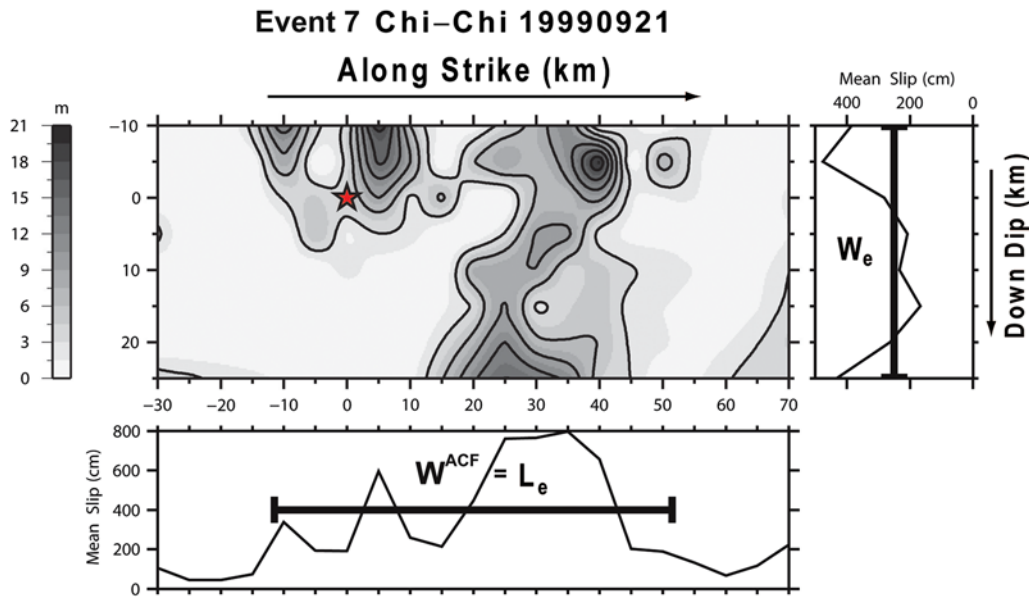
Figure 2. Illustration of how effective fault length and width were estimated from the slip model of the 1999 Chi-Chi earthquake derived from Ma *et al.* (2001). The star indicates the location of hypocenter. The amount of slip is represented by the gradient scale with 3 m contours. Two slip functions were obtained by summing the slip of each subfault along the down-dip and along strike directions and were used to obtain the effective fault width (W_e) and length (L_e), respectively. The color version of this figure is available only in the electronic edition.

scaling relationship of L_e to the seismic moment and a slope of $b = 0.40 \pm 0.05$ for the scaling relationship of W_e to the seismic moment, regardless of the fault types. A slope of $b = 0.13 \pm 0.09$ was obtained for the scaling relationship of D_e to seismic moment, suggesting a nearly constant value of mean slip within a wide range of seismic moments (10^{16} N m–10^{20} N m). Even though the events were classified into dip-slip and strike-slip types, no significant differences were found; Table 2 lists the regression parameters of all events, dip events, and strike-slip events. Previous studies (Shimazaki, 1986; Mai and Beroza, 2000; Stock and Smith, 2000) of source-scaling relationships for a constant stress drop showed the scaling of L, W, and D versus M_0 had a slope of $1/3$. Our results show that the scaling of fault dimensions versus moment has a slope of near $1/2$, suggesting they do not obey a self-similar scaling (a slope of $1/3$). Our results of scaling seismic moment to source area (A_e) give a line with slope of 0.87, rather than a slope of $2/3$ (~0.67). We considered the different values estimated from the seven published slip models for the 1999 Chi-Chi earthquake and include the minimum and maximum dimension values as error bars in Figure 3a,b. This indicates that the uncertainty determined from the various slip models did not give much bias in the scaling.

We also plotted the regression relationship derived by Mai and Beroza (2000) for comparison. Their study covers events (mostly from California) with seismic moments from 2.2×10^{17} to 1.2×10^{21} N m. The comparison of our results to the regression of Mai and Beroza (2000) shows that the effective length obtained in our study grows faster than that

in their original study. However, if we considered the events with seismic moments similar to those in Mai and Beroza (2000), the regression from their study also explains our data generally well. In addition to the events from different tectonic regimes, our study also covers much smaller events (down to the seismic moment of 10^{16} N m). These smaller events constrain the regression to have a slope of near $1/2$. Our events show larger width dimension for the regression of W_e versus M_0 than for those events used in Mai and Beroza (2000), even for events with similar seismic moments. However, for the regression of D_e versus M_0, the linear relationship derived by Mai and Beroza (2000) roughly could be seen if we specifically considered only the D_e of the earthquake with seismic moments greater than 10^{21} N m. These comparisons suggest two possibilities: (1) the necessity of conducting source-scaling studies over a wider range of seismic moments, or, (2) the possible existence of a nonlinear relationship between small and large events. However, the growth in width dimension for our events is mostly from the Taiwan orogenic belt. It might suggest the possible influence of the seismogenic regime on the scaling. More discussion of this issue is provided in the section Magnitude-Area Scaling.

Figure 4a and Figure 4b show the relationship of the mean slip to fault length and width, respectively. No significant linear trend was found in the relationship of fault dimensions (either L_e or W_e) versus mean slip, regardless of the fault types. This suggests the W model of Romanowicz (1992) or the L model of Scholz (1982) is indistinguishable for these events; that is, neither the length
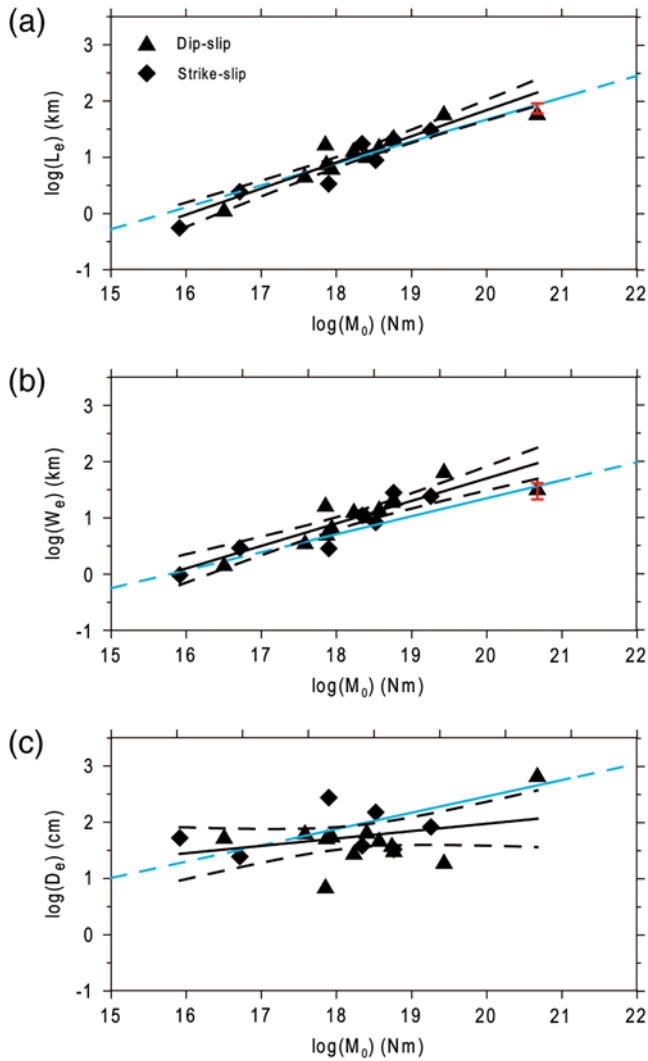
Figure 3. The scaling relationships of (a) the effective length L_e, (b) the effective width W_e, and (c) the effective mean slip D_e relative to the seismic moment M_0. The error bar for the Chi-Chi earthquake indicates the minimum and maximum effective dimension values estimated from seven Chi-Chi earthquake models (see Data and Resources section). Triangles, events of dip-slip type; diamonds, events of strike-slip type; solid lines, regression relationship shown with the value of the slope; dashed lines, the 95% confidence interval in regression; solid light line, the regression relationship of Mai and Beroza (2000) (shown for comparison); dashed light line, the extrapolation of the Mai and Beroza's regression line. The color version of this figure is available only in the electronic edition.

nor the width predominates over the evolution of slip. The correlation of the effective fault length to width (Fig. 5) shows that the growth of fault length tends to be consistent with fault width for events with rupture dimension of about 30 km. As can be seen for the 1999 M_w 7.7 Chi-Chi earthquake, the fault length becomes much larger than the fault width as width reaches a threshold of about 30 km. Two other exceptions were found for subduction zone events 18 and 19, in which the faults tended to rupture

along the dip direction of the subducting slab. Seismogenic depth might need to be considered in debating whether the fault length or width dominates the development of mean slip.

Discussion

Nonlinear Scaling of Small to Large Earthquakes

Our analyses of the scaling relationship between source dimensions and seismic moment show larger slope values than previous studies (slope of $1/3$). The fault dimensions of the smaller events help constrain the estimation of slopes. We also note the coherent growth of fault length and width for events with rupture widths less than 30 km. To explore the role of the seismogenic depth in scaling, we divided our study region into four regimes (Fig. 1) according to the specific tectonic setting in the Taiwan orogenic belt, which has the subducted slabs offshore to the northeast and southwest. Figure 6 shows the distributions of the focal depth for background seismicity in zones A–D. Most earthquakes in our analysis are located in zone C, which has seismicity to a depth of about 35 km, with the greatest concentration of seismicity at depths of 5–15 km. Unlike events in California, which have seismogenic depths of about 15 km, it appears that the seismogenic depth of 35 km in the Taiwan orogenic belt might yield the faster growth of the fault width and length for the events ruptured above the seismogenic depth. It also suggests that the locking depth might influence the developing fault width (Pacheco *et al.*, 1992; Shaw and Wesnousky, 2008).

To verify the invariance of the source scaling with fault width for large events, we expand our scaling relationship by giving four additional recent large earthquakes (the 2008 M 8.0 Wenchuan earthquake, the 2004 M 8.9 Sumatra earthquake, the 2001 M 7.8 Kunlun earthquake, and the 2001 M 7.4 Bhuj earthquake) and three large thrust earthquakes ($M_0 > 5 \times 10^{19}$ N m) from Mai and Beroza (2000) (Table 1). The slip models with effective dimensions for the four recent large earthquakes are displayed in Figure A2 of the Appendix. We also determined the effective length, width, and mean slip for these events from the referred slip models (Table 1). Except for the 2001 Kunlun earthquake, all are thrust-type events. Figure 7a–c shows the relationships of effective length, width, and mean slip versus seismic moment, with these seven additional large events (Table 1). We found two trends of linear relationships around the seismic moment of 10^{20} N m. A slope of $1/3$ fits the linear trend well for events with seismic moment greater than 10^{20} N m, both for the scaling in length and width. A similar trend was found for the scaling in D_e. These trends for the scalings with seismic moment greater than 10^{20} N m show a similar regression to those of Mai and Beroza (2000). This seems to suggest that large events have obeyed the self-similar mechanism for a constant stress drop as to satisfying the scaling relationship of $M_0 \sim L^3$.

Table 2
Constants and Coefficients of the Regression Relationships for all Events, Dip-Slip
Events, and Strike-Slip Events

$\log(Y) = a + b * \log(X)$		Slope	Standard Error	Intercept	Standard Error	Correlation Coefficient	Standard Deviation
Y	X	b	σ_b	a	σ_a	R^2	σ_y
All Events							
L_e	M_0	0.47	0.04	−7.46	0.77	0.88	0.19
W_e	M_0	0.40	0.05	−6.30	0.90	0.80	0.23
A_e	M_0	0.87	0.09	−13.79	1.63	0.85	0.41
D_e	M_0	0.13	0.09	−0.65	1.64	0.11	0.41
Dip-Slip Events							
L_e	M_0	0.42	0.06	−6.66	1.05	0.85	0.19
W_e	M_0	0.37	0.07	−5.76	1.30	0.74	0.24
A_e	M_0	0.80	0.13	−12.45	2.32	0.80	0.43
D_e	M_0	0.20	0.13	−2.01	2.32	0.20	0.43
Strike-Slip Events							
L_e	M_0	0.50	0.07	−8.11	1.20	0.92	0.20
W_e	M_0	0.42	0.08	−6.67	1.38	0.86	0.22
A_e	M_0	0.92	0.14	−14.77	2.46	0.90	0.40
D_e	M_0	0.08	0.14	0.36	2.47	0.07	0.40

However, for events with seismic moment less than 10^{20} N m, the relationship of fault dimensions to the seismic moment with slope of $1/2$ explains the data very well, and a nearly constant slip was found for these events. This constant slip, regardless of the sizes of the events, yields the scaling of $M_0 \sim L^2$. It implies these events might have variation in static stress drops and, thus, may not obey the self-similar mechanism.

Earlier studies of Shimazaki (1986), and Stock and Smith (2000) suggested an $M_0 \sim L^3$ for small earthquakes and an $M_0 \sim L^2$ for large earthquakes. Their conclusions were based on the assumptions of $W/L \sim$ constant and $D/L \sim$ constant for small earthquakes and of a near-constant value in W and $D/L \sim$ constant for large earthquakes. Our relations of $M_0 \sim L^2$ for small–moderate earthquakes are

due to the near constant of the average slip over the seismic moment, which ranged from 10^{16} to 10^{19} N m, and with $W/L \sim$ constant. For larger events, including the seven additional larger earthquakes, the scaling closely follows the Mai and Beroza scaling of $M_0 \sim L^3$ as the fault width evolves with fault length ($W/L \sim$ constant) and with $D/L \sim$ constant.

Regression Equations of Fault Dimension and Slip to the Seismic Moment

Our derived regression relationship for the effective length and width to the seismic moments for events with seismic moments smaller and greater than 10^{20} N m were derived as follows:
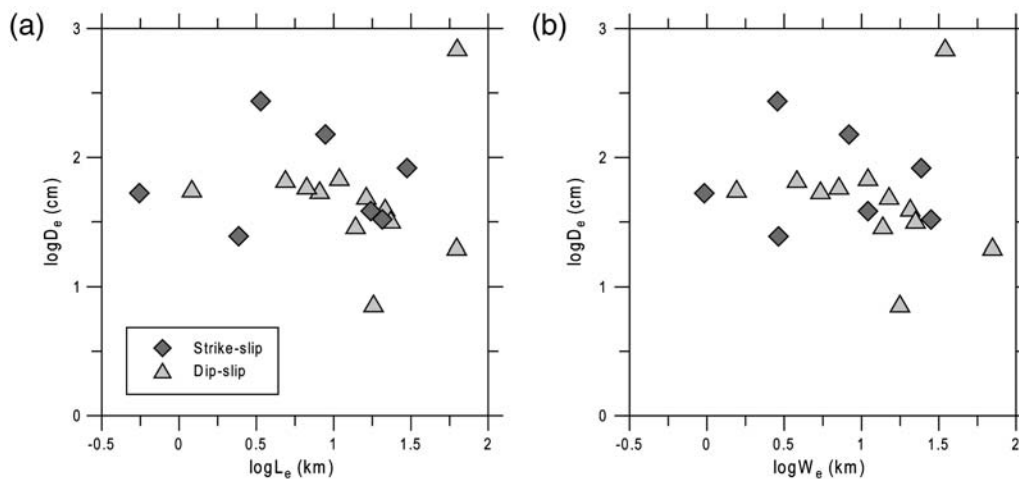

Figure 4. Comparison between the mean slip and (a) the effective length L_e and (b) the effective width W_e. Triangles, dip-slip events; diamonds, strike-slip events.
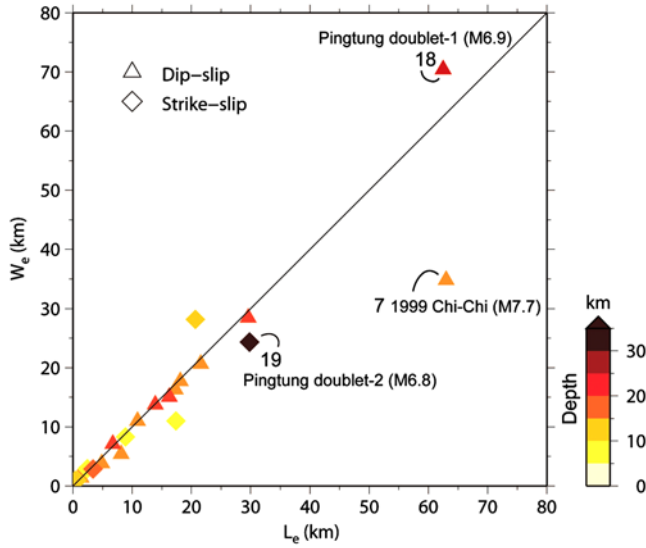
Figure 5. The correlation of the effective fault length to the effective fault width. The solid line indicates the one-to-one ratio of the effective fault length and width. Triangles, dip-slip events; diamonds, strike-slip events. The shading gradient on the symbols is related to the depths of events, as shown in the legend. The color version of this figure is available only in the electronic edition.

Figure 6. The occurrence rate with depth for the background seismicity shown in Figure 1 for (a) zone A, (b) zone B, (c) zone C, and (d) zone D. The dashed line indicates the extension of the seismicity to the depth of 35 km in zone C. The color version of this figure is available only in the electronic edition.

$$\log L_e = (1/2) \log M_0 - 8.08 \qquad (\leq 10^{20} \text{ N m})$$
$$\log W_e = (1/2) \log M_0 - 8.08$$
$$\log D_e = 1.68 \pm 0.33 \qquad\qquad\qquad (2)$$

$$\log L_e = (1/3) \log M_0 - 4.84 \qquad (> 10^{20} \text{ N m})$$
$$\log W_e = (1/3) \log M_0 - 5.27$$
$$\log D_e = (1/3) \log M_0 - 4.37 \qquad\qquad (3)$$

Wells and Coppersmith (1994) provided empirical scaling relationships from a comprehensive database of global source parameters. It has now widely been adopted for the prediction of fault dimension and slip for a given event, especially for the earthquake engineering studies. Comparing our derived regression relationships to that of Wells and Coppersmith (1994), we found the overestimation and underestimation for fault length and fault width, respectively, from their work (Table 2A in Wells and Coppersmith, 1994). The values of L_e and W_e in our regression in general are comparable to the L and W visualized directly from the slip distribution, with a difference of about 10%. The Wells and Coppersmith relationship might be able to give the upper bound of the fault dimension in length. The effective fault length from our regression gives the lower bound. However, the estimation of the fault width is strongly influenced by the seismogenic depth, and, thus, the regression relationship derived from the specific tectonic regime is essential. Another notable feature is the nearly con-
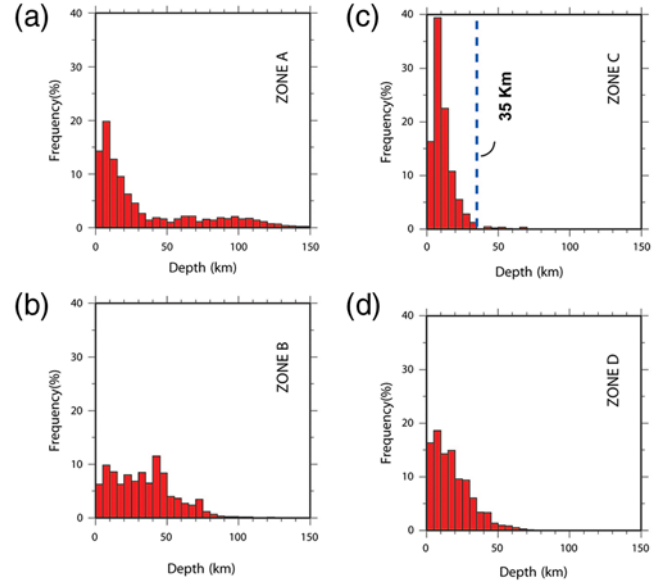
stant value of the slip over a wide range of seismic moments. This feature is important for the prediction of ground motion in earthquake engineering.

Magnitude-Area Scaling

Hanks and Bakun (2008) added an additional seven large earthquakes to the events used in Hanks and Bakun (2002) and suggested that a limitation of the seismogenic depth dominated the scaling to give the bilinear relations for fault areas larger and smaller than 537 km². According to the relationship, they agreed to a constant stress-drop model for the small events and to an *L*-model scaling for large earthquakes. Shaw (2009) gave magnitude-area scaling for small to large earthquakes by taking into account the control of the seismogenic depth, as discussed in Manighetti *et al.* (2007) on the scaling. The derived equation (8) of Shaw (2009),

$$M = \log A + \frac{2}{3} \log \frac{\max(1, \sqrt{\frac{A}{H^2}})}{[1 + \max(1, \frac{A}{H^2\beta})]/2} + \text{const.}, \qquad (4)$$

provided a good explanation of the observations of Hanks and Bakun (2008) and Wells and Coppersmith (1994). It also gave the best fit for the seismogenic depth, H, of 15.6 and for the β value of 6.9 because the data in their paper were mostly from strike-slip events in California. The β value is the scaling parameter related to the effective width as defined in Shaw (2009). Because our events mostly are thrust events from the collision zone, we explored the relation of our events to theirs by considering the seismogenic depth of
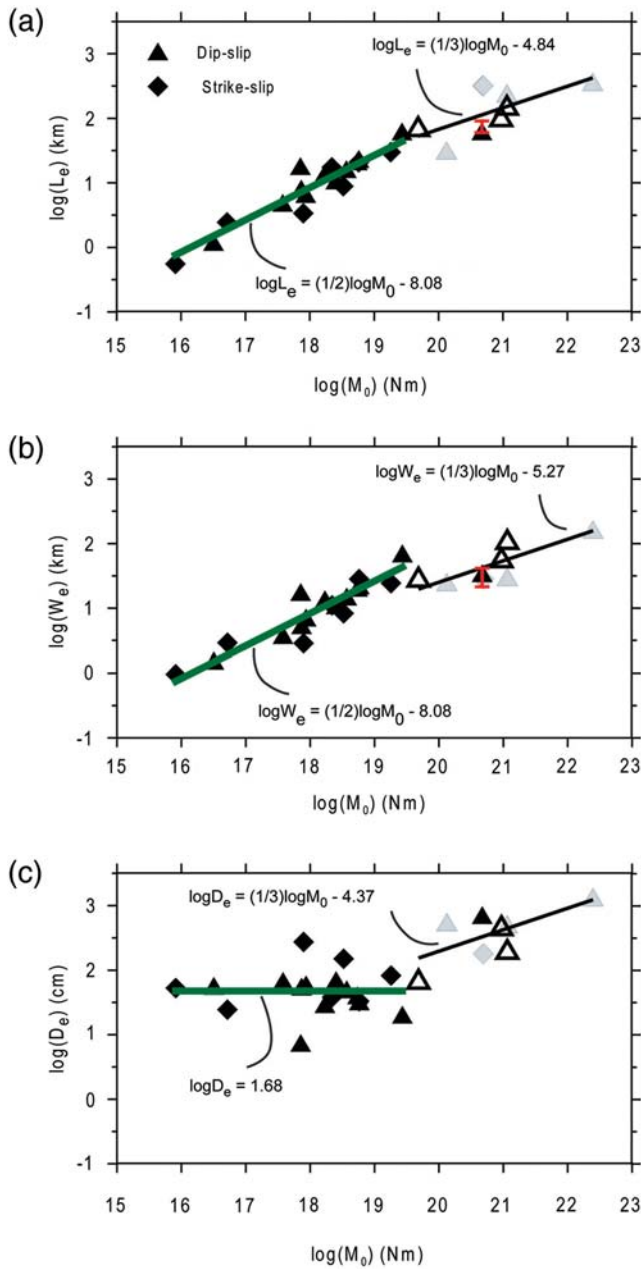
Figure 7. The scaling relationships of (a) the effective length L_e, (b) the effective width W_e, and (c) the effective mean slip D_e versus seismic moment M_0, respectively, with regressions of $M_0 \sim L^2$ for small–moderate events (thick line), and $M_0 \sim L^3$ for large events (thin line). The triangles and diamonds represent the events of dip-slip, and strike-slip types, respectively. The equations of the corresponding regression relationship of the small–moderate and large events are also shown. Light-colored triangles indicate the additional four large earthquakes used in this study (also listed in Table 1). Three large reverse events from Mai and Beroza (2000) are shown by open triangles. The deviation of the regressions for small–moderate and large events occurs at a seismic moment of about 5×10^{19} N m. The color version of this figure is available only in the electronic edition.

Taiwan as of 35 km and the β value of 6.9. Then, we made the calculations of the derived magnitude–area equation of Shaw (2009) for the different constants in equation (4).
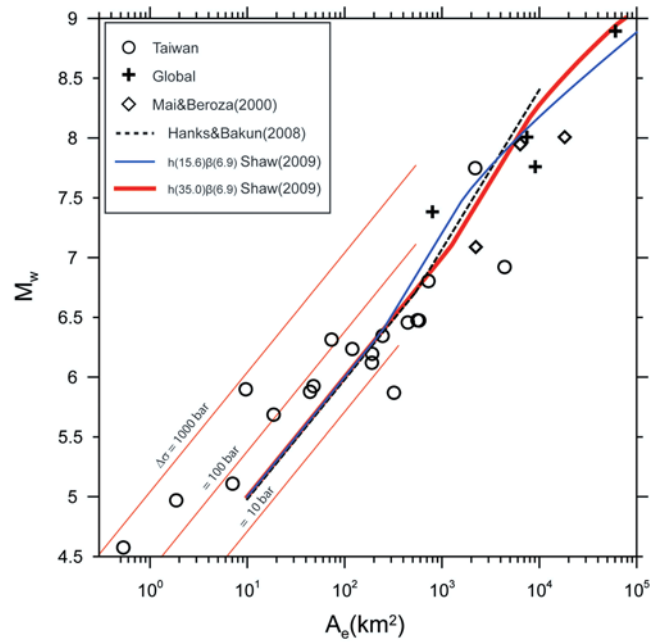
Figure 8. Illustration of magnitude–area relation. All data from Table 1 are plotted for comparison with the magnitude–area relations from Shaw (2009) with different seismogenic depth parameters and from Hanks and Bakun (2002, 2008). The thin lines show the constant stress drops ($\Delta\sigma$) of 10, 100, and 1000 bars. The color version of this figure is available only in the electronic edition.

The constants in equation (4) correspond to values of static stress drops. Here, we considered the constants related to stress drops of 10, 100, and 1000 bars, as shown in Figure 8. The spread of our events in magnitude–area plots suggests the possible variance in stress drops for these events. However, if we considered only events with stress drops of 10–100 bars, we obtained a regression on magnitude–area scaling that fit the data well. This shows a first bilinear feature at a fault area of about 1000 km², similar to the bilinear features observed in Figure 7a and 7(b). Shaw (2009) suggested that the two bilinear features in the scaling agree to the $\log A$ scaling at small magnitudes, L model scaling of $4/3 \log A$ for moderate large events, and a W model scaling of $2/3 \log A$ for the very largest events. For the events with stress drops of 10–100 bars, our observations related to Shaw's equation suggest support for the derived magnitude–area scaling of Shaw (2009) by considering the thicker seismogenic depth for the thrust events in the collision zone. As compared to the regression of Hanks and Bakun (2008) and Shaw (2009), which considered a variety of strike-slip events from various places (including many from California), our regression shows further extension of the first bilinear relations to a greater area because the growth of collision zone events have wider extensions in fault width due to the thicker seismogenic depth. For events with stress drops of 10–100 bars, our regression gives an average stress drop of about 28 bars (similar to most of the observations of about

30 bars) and, with an *L*-model scaling, $D = \alpha L$, with the scaling parameter α of 1.7×10^{-5} for events with rupture dimension greater than the seismogenic depth. The mega thrust of the 2004 Sumatra earthquakes was well scaled by a third regression line. However, a notable feature of the plot is that three events have relatively high stress drops, as much as several hundreds bars.

Stress Drops

Although our regression on the magnitude–area relationship supports the near-constant stress drop for small earthquakes, there are three events with large stress drops that were excluded from our discussion. Because our studies on scaling for events with seismic moment less than 10^{20} N m suggested possible variation in static stress drops of these events, we made a further study of the static stress drops of these events. For a circular fault, seismic moment can be related to fault area and stress drop by (Kanamori and Anderson, 1975)

$$\log M_0 = \frac{3}{2} \log A + \log \left(\frac{16}{7\pi^{3/2}} \Delta\sigma \right), \qquad (5)$$

where M_0 is the seismic moment; A is the fault area, and $\Delta\sigma$ is the static stress drop. We used the effective fault area (A_e) to estimate the corresponding stress drops of these events (Table 1). Figure 9 shows the relationship between the logarithm of the effective area and seismic moment with various stress drops of 1, 10, 100, and 1000 bars. As shown earlier in this article, most of the events have stress drops between 10 to 100 bars, similar to common observations such as in Kanamori and Anderson (1975). However, events with seismic moments less than 10^{20} N m seem to have an inverse relation between earthquake size and stress drops. Nevertheless, the events 2, 5, and 16 appear to have very high stress drops (up to hundreds of bars), despite their relatively smaller magnitudes.

Allmann and Shearer (2009) suggested that the strike-slip earthquakes might have larger stress drop than those for normal and thrust-type mechanisms. Hardebeck and Aron (2009) found that high stress drops occur in a deep cluster of thrust-faulting earthquakes; however, no direct correlation of the large stress drop with fault type was found in our study. Several studies (Asano *et al.*, 2003; Allmann and Shearer, 2009; Hardebeck and Aron, 2009) also discussed whether the stress drops of the events vary systematically with depth. Our data set did not reveal a systematic trend of stress drops with depth either. However, the very high stress drops of these three events might indirectly imply a complex stress field in the Taiwan orogenic belt. Kanamori *et al.* (1990; 1993) and Ma and Kanamori (1994) also found very high stress drop, as shown in Figure 9 for the 1988 Pasadena earthquake and the 1991 Sierra Madre earthquake, which occurred in the Transverse Ranges and the Los Angeles basin in California. They suggested that the occurrence of these high stress drop events
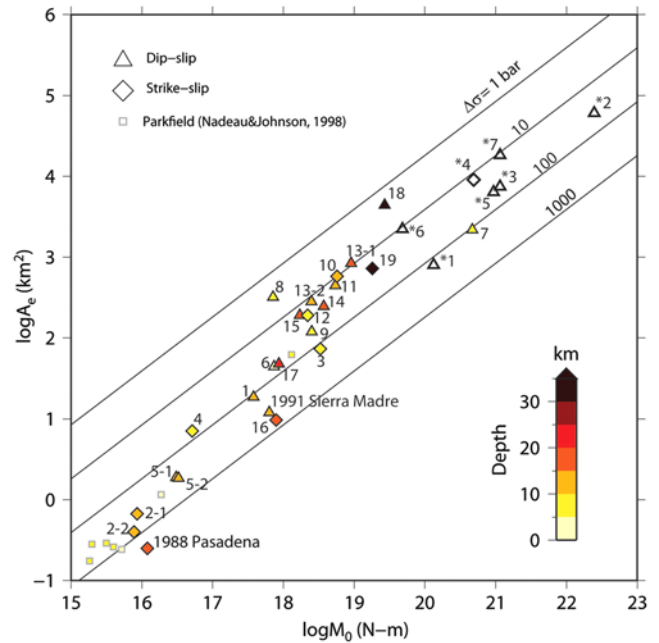

Figure 9. The relationship of the logarithm of effective area (A_e) to the logarithmic of seismic moment (M_0). The straight lines represent the constant stress drop ($\Delta\sigma$) of 1, 10, 100, and 1000 bars, respectively, under a circular crack model. The triangles and diamonds represent the dip-slip and strike-slip types of events, respectively, and the shading gradient indicates the depth of the events as shown in the legend. The numbers by each symbol correspond to the events listed in Table 1. Open triangles indicate the four additional large events and three events from Mai and Beroza (2000). Squares indicated the Parkfield repeating events from Nadeau and Johnson (1998). The color version of this figure is available only in the electronic edition.

near the base of the seismogenic zone might indicate that these fault systems are capable of supporting high stress that will eventually be released in major seismic events and thus give important implications for the regional seismic potential.

The inverse relation of the stress drops to the earthquake size is intriguing. Nadeau and Johnson (1998) examined Parkfield repeating events and suggested very high stress drops of these repeating events, with a general trend that also showed an inverse relation of the stress drop to event size. The static stress drops of these events are shown together with our events in Figure 9. Our observations, compared with Parkfield's, seem to suggest stress drops of within 10–100 bars for most of events with seismic moment greater than $\sim 10^{17}$–10^{18} N m. However, events with seismic moment less than this range tend to have larger stress drops. This might imply a high heterogeneity of stress distribution within the crust. Several small events came from the localized high-stress patches.

The three high stress drop events we observed in Taiwan were located near the frontal faults of the fold-and-thrust belt of the Taiwan orogenic zone (Fig. 1). The focal depths of these events are much deeper than the depth of the decollement of about 7 km (Carena *et al.*, 2002), suggesting

these events are from the blind faults. As with the very high stress drop events observed from the Transverse Ranges and the Los Angeles basin of California, these high stress drops events might give a relatively higher peak ground acceleration (PGA) due to large slip on a small asperity and, thus, have more potential for seismic hazard than similar size events in a different tectonic setting.

Comparison of the PGA Attenuation to Next Generation Attenuation (NGA) Model

To examine the possibility of the high stress drop events yielding high PGAs, we determined the PGA attenuation for high stress drop events 2, 5, and 16 and for event 6, which has a regular stress drop of about 61 bars, for comparison (Fig. 10a–10d). We based the PGA attenuation on the derived attenuation model of Taiwan by Liu and Tsai (2005) and the recently developed NGA model of Lin (2009). Lin (2009)

referred to the model of the NGA Ground Motions Project of the Pacific Earthquake Engineering Research Center to build the attenuation model for the Taiwan region. The major modification in Lin (2009) for improving the previous attenuation models of Taiwan was to add the site effect factor into their attenuation model through the adoption of site classification based on the shear wave velocity (V_{S30}) of the top 30 m. For inspecting the possible site effects on PGA, V_{S30} was set to a shear velocity of 180 cm/s in soft soil for the maximum effect (Lee and Tsai, 2008). Comparing the observed PGA with the predicted attenuation models provided by Lin (2009) and Liu and Tsai (2005), the observed PGAs in the near-field as a hypocenter distance of less than 20–30 km are much larger than the predicted PGAs in both models, as seen in Figure 10a–c for events, 2, 5, and 16, respectively. To investigate the possible influence of these high PGAs from site effect, we determined the PGA attenuation for regular event 6, as seen in Figure 10d, with the stations denoted
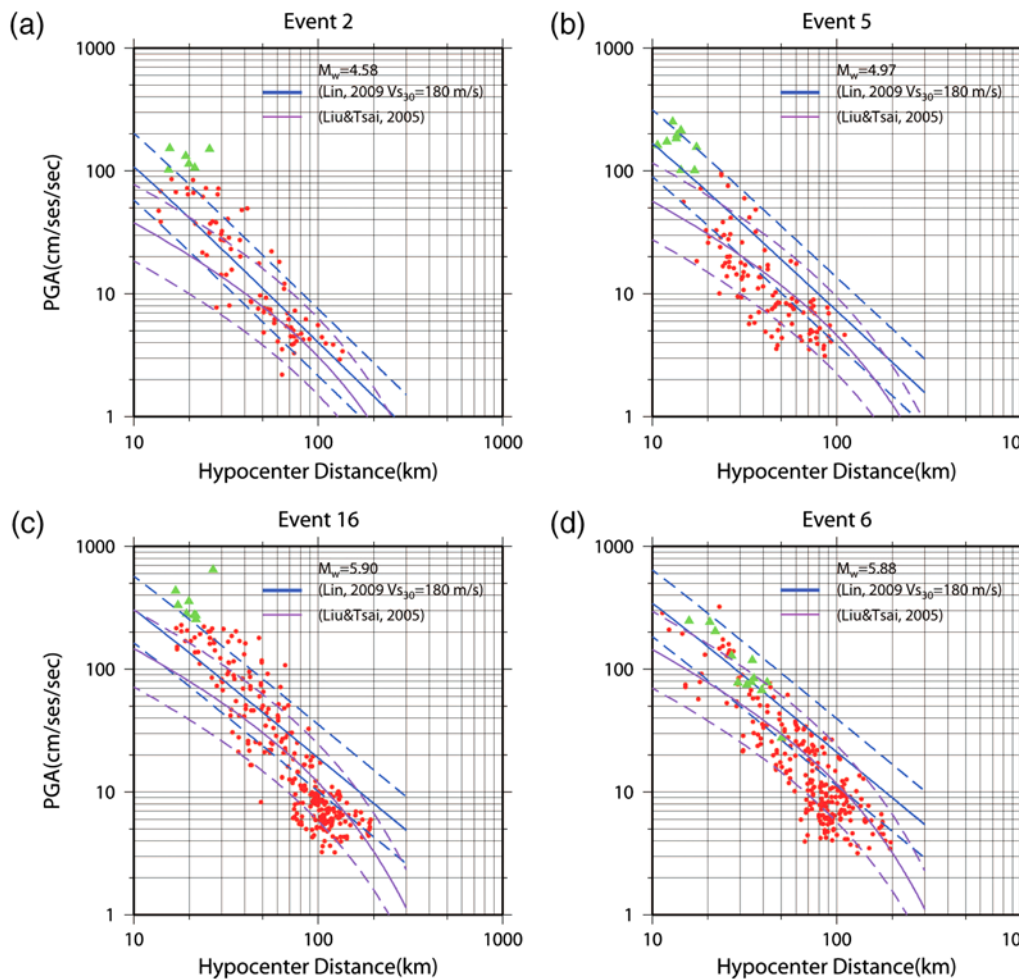

Figure 10. Comparison of the observed horizontal PGA with the two attenuation models of Lin (2009) and Liu and Tsai (2005) represented by the solid thick and thin lines, respectively, for (a) event 2, (b) event 5, (c) event 16, and (d) event 6. The dashed lines indicate the range of the standard deviation. The PGA values of the stations are shown by circles. The triangles are the stations with PGA values greater than 100 cm/s/s for events 2 and 5 and with PGA value greater than 250 cm/s/s for event 16. The triangles shown in event 6 are PGA values of stations that are common to events 2, 5, and 16. The color version of this figure is available only in the electronic edition.

by triangles indicating the common stations with the high PGA in events 2, 5, and 16. The common stations, which have high PGA in events 2, 5, and 16, now have the values within the general trend of the PGA attenuation of event 6. These observations ruled out the possibility of the site effect inducing the observed high PGA from the high stress drop events and implied the high stress drops caused the high PGA. Current seismic hazard analysis considers events only down to M 5.5, our study shows that, regardless of the smaller magnitude, high stress drop events will yield localized high PGA and thus will require special attention in seismic hazard mitigation. Radiguet *et al.* (2009) suggest the dependence of near-field ground motions on the structural maturity of ruptured faults. Events from immature faults tend to have higher stress drops. Our observations that the events with larger stress drops were mainly from blind faults below the decollement in western Taiwan appear to be in agreement with their observations.

Conclusions

We have analyzed the scaling relationships between source parameters (L_e, W_e, and D_e) and seismic moment from 19 inverted finite-fault models (12 dip-slip, 7 strike-slip) in the Taiwan region. Seven additional larger events were considered to provide better constraint to the scaling of larger events. Our results show the influence of the seismogenic depth on the development of the fault dimension during rupture. An equal increase of effective fault length and width was found for earthquakes in which the ruptured dimension occurs within the seismogenic thickness, such as occurs in the 35-km-deep region of the Taiwan region. For this case, a nearly constant value of the slip was observed regardless of the size of the events. Two trends of scaling of $M_0 \sim L^2$ and $M_0 \sim L^3$ were observed, respectively, for the seismic moment smaller than and greater than 10^{20} N m. Although the events showed some variation in stress drops (except three events with high stress drops), most of the events had stress drops of 10–100 bars. This bilinear relation was well explained by the derived magnitude–area equation of Shaw (2009) when we considered only events with stress drops of 10–100 bars and a seismogenic thickness of 35 km. The bilinear feature of the regressed magnitude–area scaling appears at a ruptured area of about 1000 km^2, for a seismogenic thickness of 35 km. For the events having a rupture area larger than that, the amount of the average slip becomes proportional to the rupture length. The derived magnitude–area scaling of Shaw (2009), with the consideration of seismogenic depth, explains the data well for the events with stress drops of 10–100 bars. This comparison suggests seismogenic thickness controls earthquake scaling. However, several distinct events with the seismic moment less than 10^{19} N m show very high stress drops of up to hundreds of bars. The distinct high stress drop events yield local high PGA, as determined from comparison to the NGA model. These events, mainly

from buried faults in the fold-and-thrust belt of the orogenic zone, will require special attention because they had small fault dimensions ($A_e < 10$ km^2) but large slip (up to 1 m). These result in relatively larger PGAs, despite their small–moderate magnitude. An empirical relationship for different tectonic regimes, especially a consideration of the influence of the seismogenic thickness, is necessary for earthquake engineering analysis. Although most of the attention is to the scaling of larger earthquakes, small to moderate size events of $M_w \sim 6.5$ from the buried faults in Taiwan region still require special attention for seismic hazard mitigation.

Data and Resources

Acknowledgments

References

Allmann, B. P., and P. M. Shearer (2009). Global variations of stress drop for moderate to large earthquakes, *J. Geophys. Res.* **114,** no. B01310, doi 10.1029/2008JB005821.

Ammon, C. J., C. Ji, H. K. Thio, D. Robinson, N. Sidao, V. Hjorleifsdottir, H. Kanamori, T. Lay, S. Das, D. Helmberger, G. Ichinose, J. Polet, and D. Wald (2005). Rupture process of the 2004 Sumatra–Andaman earthquake, *Science* **308,** 1133–1139, doi 10.1126/science.1112260.

Antolik, M., and D. S. Dreger (2003). Rupture process of the 26 January 2001 M_w 7.6 Bhuj, India, earthquake from teleseismic broadband data, *Bull. Seismol. Soc. Am.* **93,** 1235–1248.

Asano, K., T. Iwata, and K. Irikura (2003). Source characteristics of shallow intraslab earthquakes derived from strong-motion simulations, *Earth Planets Space* **55,** 5–8.

Bracewell, R. N. (1986). *The Fourier Transform and Its Applications*, McGraw-Hill, New York.

Carena, S., J. Suppe, and H. Kao (2002). Active detachment of Taiwan illuminated by small earthquakes and its control of first-order topography, *Geology* **30,** 935–938.

Chi, W. C., and D. Dreger (2004). Crustal deformation in Taiwan: Results from finite source inversions of six M_w > 5.8 Chi-Chi aftershocks, *J. Geophys. Res.* **109,** no. B07305, doi 10.1029/2003JB002606.

Hanks, T. C., and W. H. Bakun (2002). A bilinear source-scaling model for M-$\log A$ observations of continental earthquakes, *Bull. Seismol. Soc. Am.* **92,** 1841–1846.

Hanks, T. C., and W. H. Bakun (2008). *M*-log *A* observations for recent large earthquakes, *Bull. Seismol. Soc. Am.* **98,** 490–494.

Hardebeck, J. L., and A. Aron (2009). Earthquake stress drops and inferred fault strength on the Hayward fault, east San Francisco Bay, California, *Bull. Seismol. Soc. Am.* **99,** 1801–1814.

Hartzell, S. H., and T. H. Heaton (1983). Inversion of strong ground motion and teleseismic waveform data for the fault rupture history of the 1979 Imperial Valley, California, earthquake, *Bull. Seismol. Soc. Am.* **73,** 1553–1583.

Ji, C. (2008). Preliminary result of the May 12, 2008 M_w 7.97 Sichuan earthquake,, http://www.geol.ucsb.edu/faculty/ji/big_earthquakes/2008/05/12/ShiChuan.html (last accessed 22 February 2010).

Kanamori, H., and D. L. Anderson (1975). Theoretical basis of some empirical relations in seismology, *Bull. Seismol. Soc. Am.* **65,** 1073–1095.

Kanamori, H., J. Mori, and T. H. Heaton (1990). The 3 December 1988, Pasadena earthquake ($M_L = 4.9$) recorded with the very broadband system in Pasadena, *Bull. Seismol. Soc. Am.* **80,** 483–487.

Kanamori, H., J. Mori, E. Hauksson, T. Heaton, L. K. Hutton, and L. M. Jones (1993). Determination of earthquake energy released and M_L using Terrascope, *Bull. Seismol. Soc. Am.* **83,** 330–346.

Lee, C. T., and B. R. Tsai (2008). Mapping V_{s30} in Taiwan, *Terr. Atmos. Ocean. Sci.* **19,** 671–682.

Lin, H. I. (2004). Earthquake source scaling of moderate to large earthquakes in Taiwan: Study of 2003 $M_w > 6$ Taiwan earthquakes, *M.Sc. Thesis*, National Central University, Taiwan, 95 pp. (in Chinese).

Lin, P. S. (2009). Ground-motion attenuation relationship and path-effect study using Taiwan data set, *Ph.D. Dissertation*, National Central University, Taiwan, 157 pp. (in Chinese).

Liu, K. S., and Y. B. Tsai (2005). Attenuation relationships of peak ground acceleration and velocity for crustal earthquakes in Taiwan, *Bull. Seismol. Soc. Am.* **95,** 1045–1058.

Ma, K. F., and H. Kanamori (1994). Broadband waveform observation of the 28 June 1991 Sierra Madre earthquake sequence ($M_L = 5.8$), *Bull. Seismol. Soc. Am.* **84,** 1725–1738.

Ma, K. F., J. Mori, S. J. Lee, and S. B. Yu (2001). Spatial and temporal distribution of slip for the 1999 Chi-Chi, Taiwan, earthquake, *Bull. Seismol. Soc. Am.* **91,** 1069–1087.

Ma, K. F., and H. Y. Wu (2001). Quick slip distribution determination of moderate to large inland earthquakes using near-source strong motion waveforms, *Earthq. Eng. Eng. Seismol.* **3,** 1–10.

Mai, P. M., and G. C. Beroza (2000). Source scaling properties from finite-fault-rupture models, *Bull. Seismol. Soc. Am.* **90,** 604–615.

Manighetti, I., M. Campillo, S. Bouley, and F. Cotton (2007). Earthquake scaling, fault segmentation, and structural maturity, *Earth Planet. Sci. Lett.* **253,** 429–438.

Mendoza, C., and S. H. Hartzell (1989). Slip distribution of the 19 September 1985 Michoacan, Mexico, earthquake: Near-source and teleseismic constraints, *Bull. Seismol. Soc. Am.* **79,** 655–669.

Nadeau, R. M., and L. R. Johnson (1998). Seismological studies at Parkfield VI: Moment release rates and estimates of source parameters for small repeating earthquakes, *Bull. Seismol. Soc. Am.* **88,** 790–814.

Pacheco, J. F., C. H. Scholz, and L. R. Sykes (1992). Changes in frequency—size relationship from small to large earthquakes, *Nature* **355,** 71–73.

Pegler, G., and S. Das (1996). Analysis of the relationship between seismic moment and fault length for large crustal strike-slip earthquakes between 1977–92, *Geophys. Res. Lett.* **23,** 905–908.

Radiguet, M., F. Cotton, I. Manighetti, M. Campillo, and J. Douglas (2009). Dependency of near-field ground motions on the structural maturity of the ruptured faults, *Bull. Seismol. Soc. Am* **99,** 2572–2581.

Romanowicz, B. (1992). Strike-slip earthquakes on quasi-vertical transcurrent faults: Inferences for general scaling relations, *Geophys. Res. Lett.* **19,** 481–484.

Scholz, C. H. (1982). Scaling laws for large earthquakes: Consequences for physical models, *Bull. Seismol. Soc. Am.* **72,** 1–14.

Scholz, C. H. (1994). A reappraisal of large earthquake scaling, *Bull. Seismol. Soc. Am.* **84,** 215–218.

Shaw, B. E. (2009). Constant stress drop from small to great earthquakes in magnitude-area scaling, *Bull. Seismol. Soc. Am.* **99,** 871–875.

Shaw, B. E., and S. G. Wesnousky (2008). Slip-length scaling in large earthquakes: The role of deep-penetrating slip below the seismogenic layer, *Bull. Seismol. Soc. Am.* **98,** 1633–1641.

Shimazaki, K. (1986). Small and large earthquakes: The effects of the thickness of seismogenic layer and the free surface, in *Earthquake Source Mechanics*, Das, S., J. Boatwright, and C. H. Scholz (Editors), American Geophysical Monograph **37**, 209–216.

Stock, C., and E. G. C. Smith (2000). Evidence for different scaling of earthquake source parameters for large earthquakes depending on faulting mechanism, *Geophys. J. Int.* **143,** 157–162.

Wald, D. J., and T. H. Heaton (1994). Spatial and temporal distribution of slip for the 1992 Landers, California, earthquake, *Bull. Seismol. Soc. Am.* **84,** 668–691.

Wald, D. J., D. V. Helmberger, and T. H. Heaton (1991). Rupture model of the 1989 Loma Prieta earthquake from the inversion of strong-motion and broadband teleseismic data, *Bull. Seismol. Soc. Am.* **81,** 1540–1572.

Wang, J. H., and S. S. Ou (1998). On scaling of earthquake faults, *Bull. Seismol. Soc. Am.* **88,** 758–766.

Wells, D. L., and K. J. Coppersmith (1994). New empirical relationships among magnitude, rupture length, rupture width, rupture area, and surface displacement, *Bull. Seismol. Soc. Am.* **84,** 974–1002.

Wen, Y. Y., K. F. Ma, T. R. A. Song, and W. D. Mooney (2009). Validation of the rupture properties of the 2001 Kunlun, China ($M_s = 8.1$), earthquake from seismological and geological observations, *Geophys. J. Int.* **177,** 555–570.

Wessel, P., and W. H. F. Smith (1998). New, improved version of generic mapping tools released, *EOS Trans. AGU* **79,** 579.

Wu, C. J., M. Takeo, and S. Ide (2001). Source process of the Chi-Chi earthquake: A joint inversion of strong motion data and global positioning system data with a multifault model, *Bull. Seismol. Soc. Am.* **91,** 1128–1143.

Yen, Y. T. (2002). Slip distribution of $M_w > 6.0$ aftershocks of the 1999 Chi-Chi Taiwan earthquake, *M.Sc. Thesis*, National Central University, Taiwan, 122 pp. (in Chinese).

Yen, Y. T., K. F. Ma, and Y. Y. Wen (2008). Slip partition of the 26 December 2006 Pingtung, Taiwan (*M* 6.9, *M* 6.8) earthquake doublet determined from teleseismic waveforms, *Terr. Atmos. Ocean. Sci.* **19,** 567–578.

Yin, Z. M., and G. C. Rogers (1996). Toward a physical understanding of earthquake scaling relations, *Pure Appl. Geophys.* **146,** 661–675.

Zeng, Y. H., and C. H. Chen (2001). Fault rupture process of the 20 September 1999 Chi-Chi, Taiwan, earthquake, *Bull. Seismol. Soc. Am.* **91,** 1088–1098.

Appendix

The spatial slip distribution of the 19 finite-fault models (Fig. A1) in the Taiwan region and 4 additional large earthquakes (Fig. A2) are listed in Table 1. The slip models for two fault planes for events 2, 5, and 13 are also shown. The estimated effective length and width (shown by a bar with units in km), calculated from the slip distribution along the strike direction and dip direction, are also depicted in the slip model. For an objective analysis, slip distributions
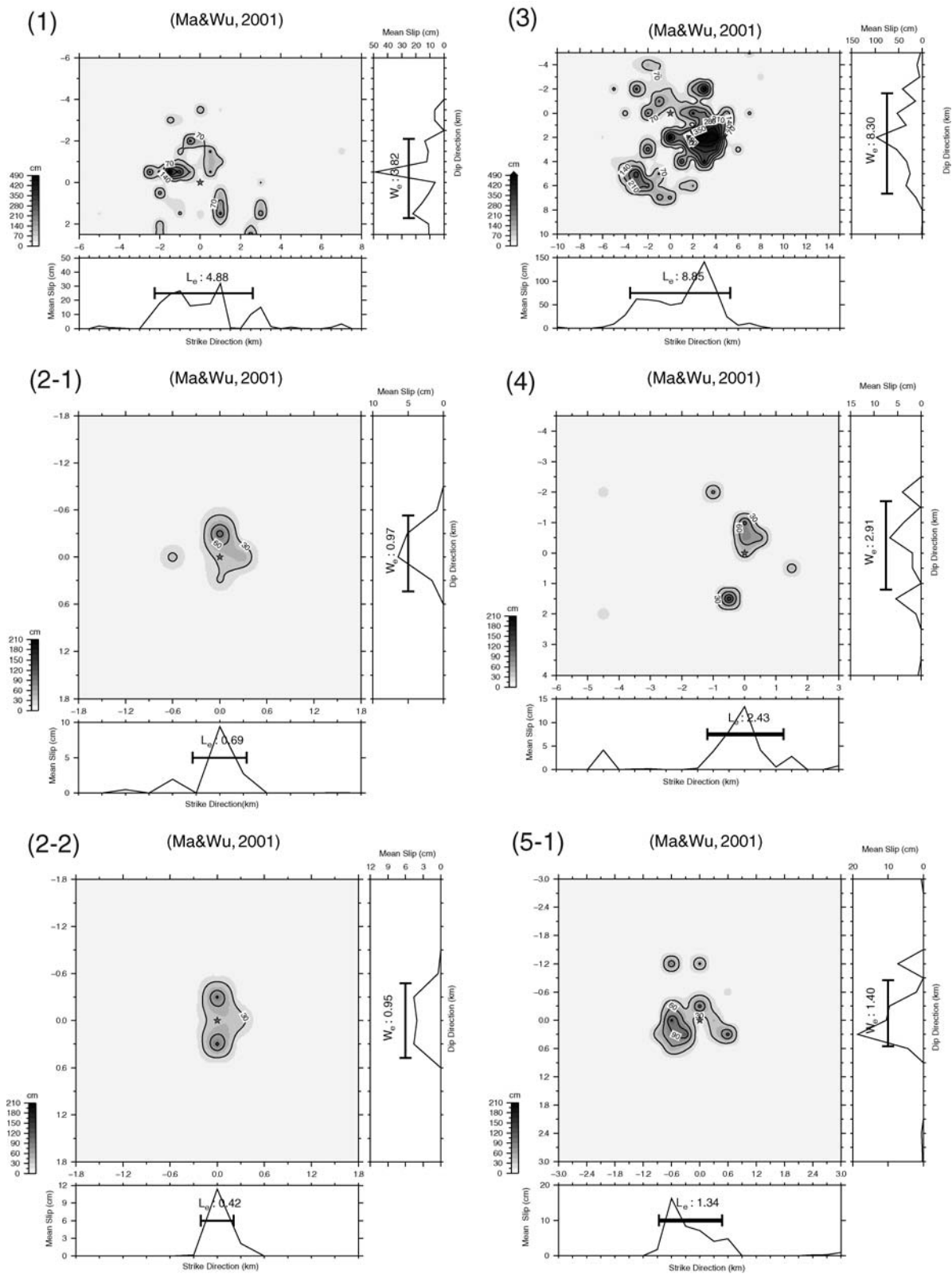
Figure A1. Spatial slip distribution of the 19 referred finite-fault models in the Taiwan region. Numbers in upper left corner of each panel correspond to data in Table 1. *(Continued)*
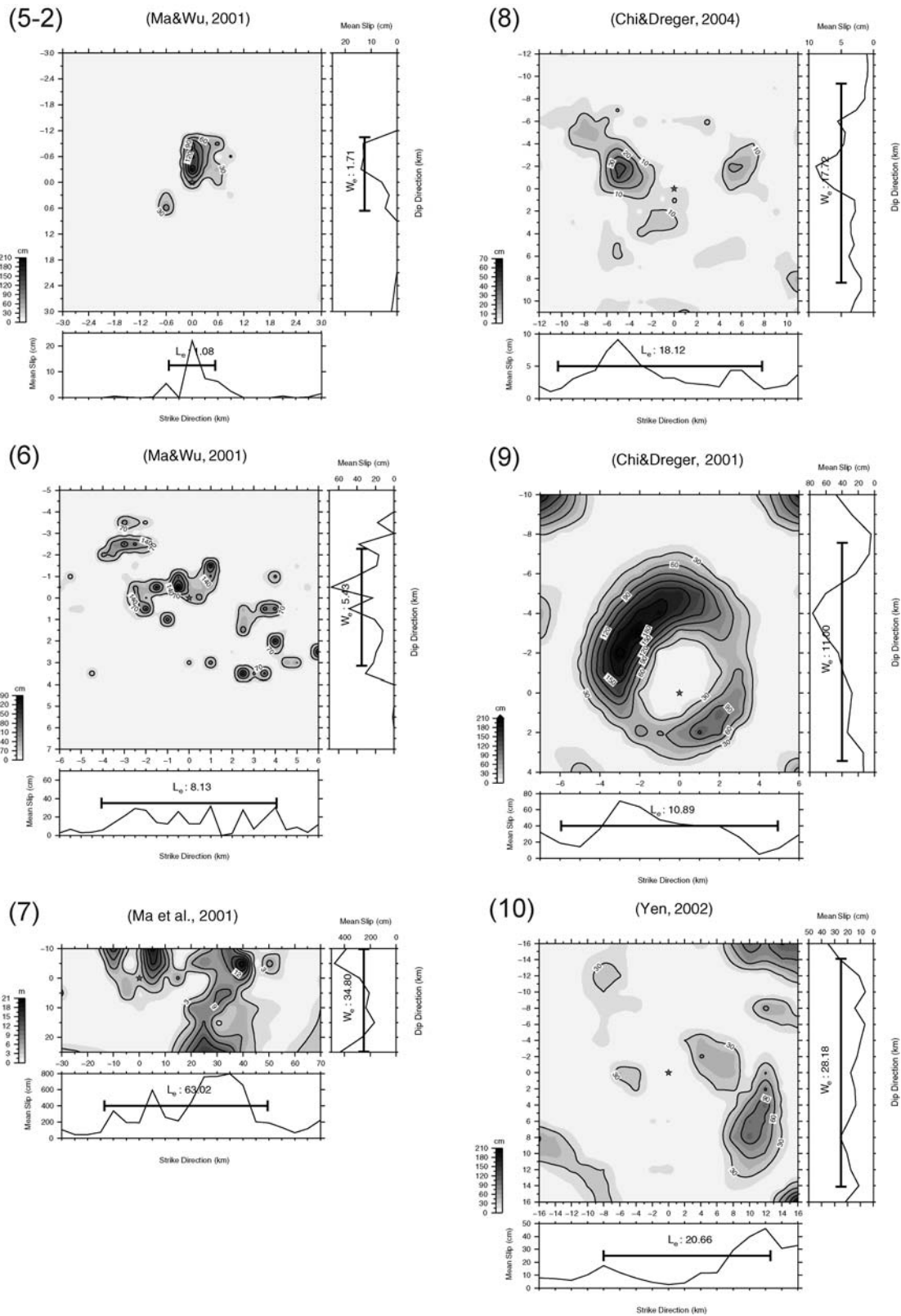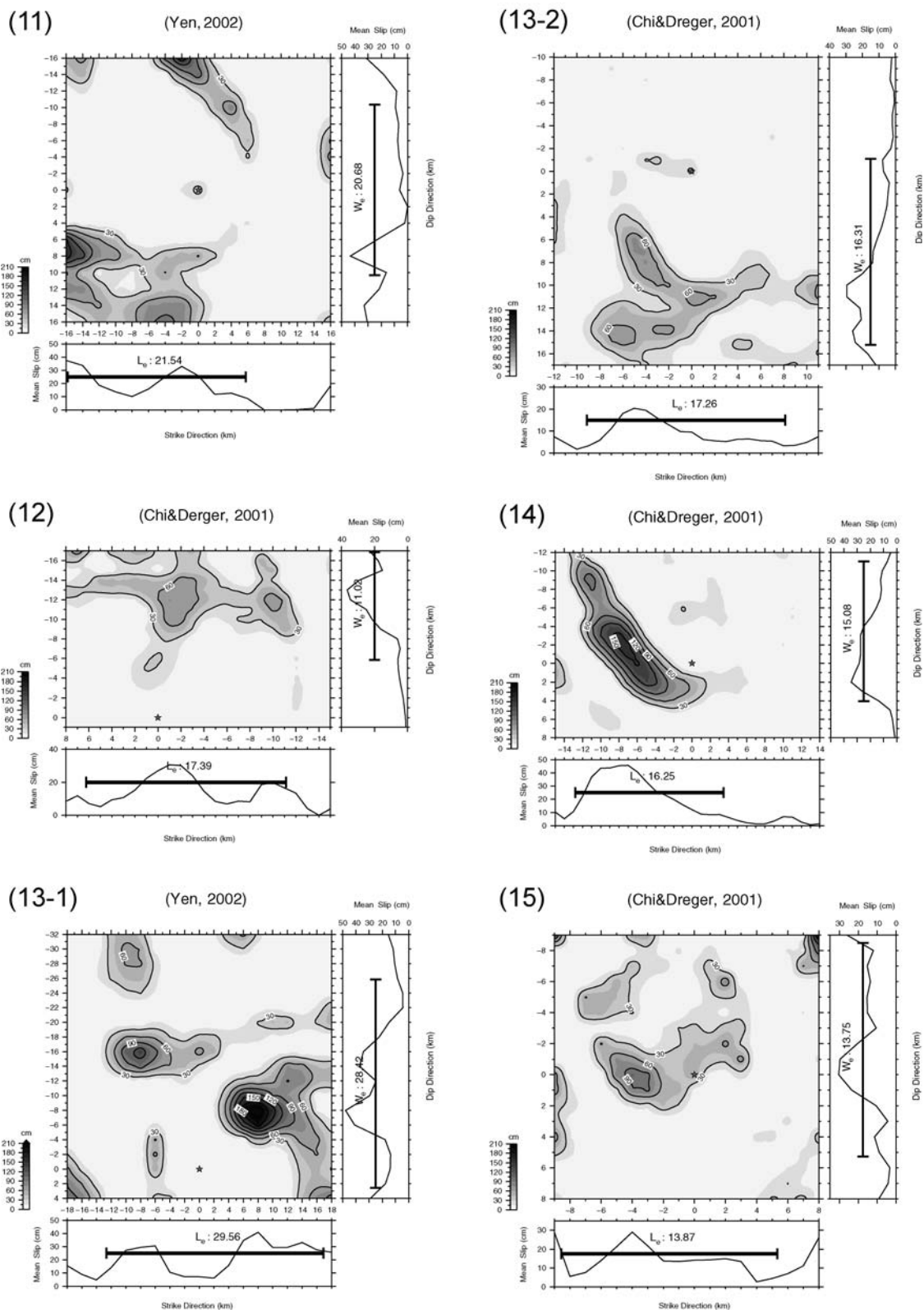
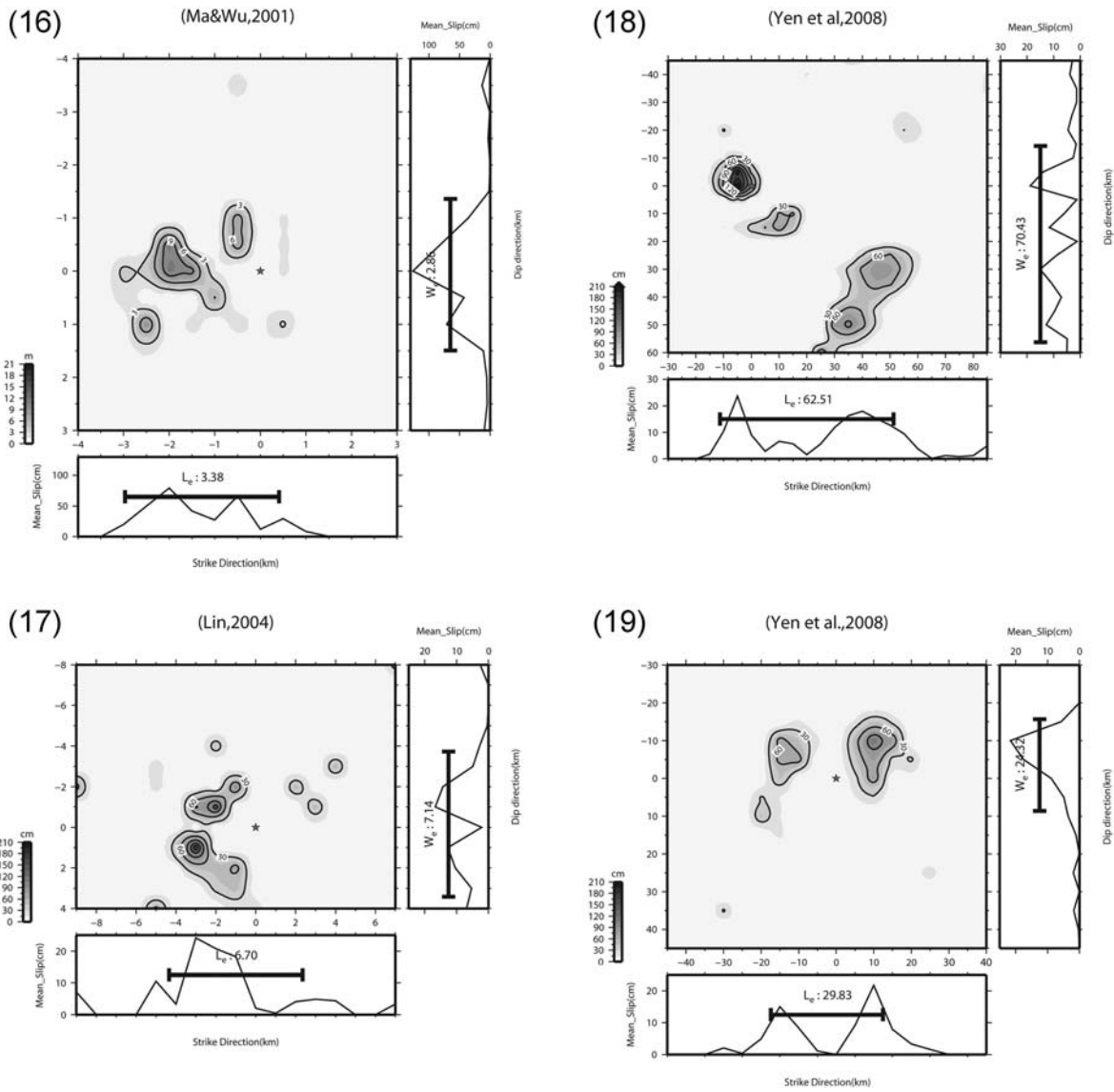**Figure A1.** Continued.

Figure A1. Continued.
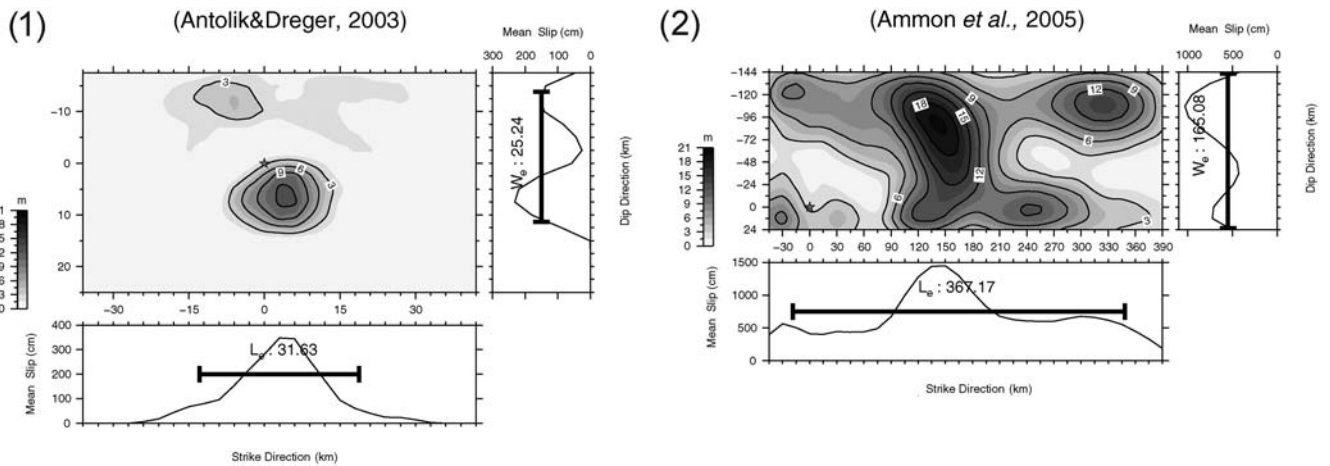
Figure A1. Continued.

Figure A2. Spatial slip distribution of four additional large earthquakes in the Taiwan region. Numbers in upper left corner of each panel correspond to the event numbers in bold type in Table 1.   (*Continued*)
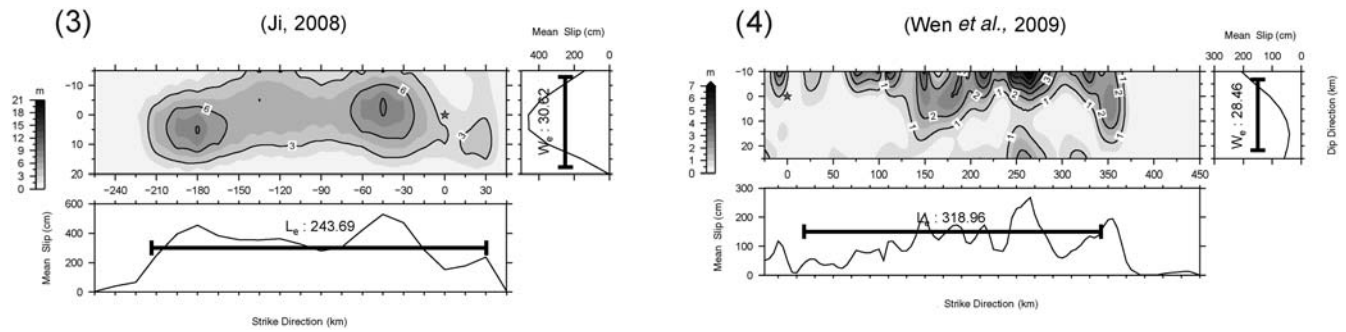
Figure A2. Continued.

of the slip models collected from various references were kept in their original form.

The number shown at the left for each slip model corresponds to the event listed in Table 1. Note that slip is scaled differently for different events, as indicated by the scale at the lower left of each model.

Institute of Geophysics
National Central University
No. 300, Jhongda Rd., Jhongli City
Taoyuan County 320, Taiwan
fong@eqkc.earth.ncu.edu.tw